A Virtual Synchronous Machine implementation for distributed control of power converters in SmartGrids

3 authors, including:

Jon Are Suul
Norwegian University of Science and Technology
154 PUBLICATIONS **4,554** CITATIONS

Olav Bjarte Fosso
Norwegian University of Science and Technology
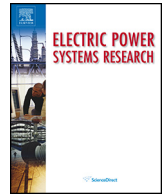**157** PUBLICATIONS **2,079** CITATIONS

Some of the authors of this publication are also working on these related projects:

Instantaneous Frequency in Electric Power Systems View project

CIGRE B4 View project

A Virtual Synchronous Machine implementation for distributed control of power converters in SmartGrids

Salvatore D'Arco [a], Jon Are Suul [a,b,*], Olav B. Fosso [b]

[a] SINTEF Energy Research, 7465 Trondheim, Norway
[b] Department of Electric Power Engineering, Norwegian University of Science and Technology, 7495 Trondheim, Norway

ABSTRACT

The ongoing evolution of the power system towards a "SmartGrid" implies a dominant role of power electronic converters, but poses strict requirements on their control strategies to preserve stability and controllability. In this perspective, the definition of decentralized control schemes for power converters that can provide grid support and allow for seamless transition between grid-connected or islanded operation is critical. Since these features can already be provided by synchronous generators, the concept of Virtual Synchronous Machines (VSMs) can be a suitable approach for controlling power electronics converters. This paper starts with a discussion of the general features offered by the VSM concept in the context of SmartGrids. A specific VSM implementation is then presented in detail together with its mathematical model. The intended emulation of the synchronous machine characteristics is illustrated by numerical simulations. Finally, stability is assessed by analysing the eigenvalues of a small-signal model and their parametric sensitivities.

1. Introduction

The increasing penetration of power generation from renewable energy sources and the transition from a centralized power production model to distributed generation are expected to pose serious challenges to the development and operation of future power systems. This tendency is a strong motivation behind the paradigm shift from the traditional power system architecture towards an approach ensuring more flexibility and coordination between the generation units and loads that is promised by "SmartGrids" [1]. At the same time, the share of the electric power transferred through the power system which is processed by at least one power electronic conversion stage in the path from primary energy conversion to final consumption is continuously increasing. Already in 2007, it was estimated that this share would reach 80% around 2015 [2], and even if the development has been slightly slower, such a high share of power electronic conversion is expected to be exceeded during the coming years. Thus, power electronic control will have a crucial role in the emerging SmartGrid scenario, as the presence of power converters in the power system and their impact on global stability and controllability continues to increase.

Although the ongoing SmartGrid developments point towards an increasing level of communication and integration between various elements of the power system, distributed architectures with local primary control of converters combined with centralized secondary control seem to be an appropriate approach for optimizing steady-state operation while ensuring immediate response to transient events. Thus, converter units should be able to react autonomously to abrupt changes in the power system operating conditions, while complying on a longer time scale with the set-points and service requirements requested by the system operator through external communication.

In classical power systems, the Synchronous Machine (SM) with speed governor and excitation control offers favourable features to support the system operation within a distributed control scheme. Indeed, SMs contribute to the system damping through their inertia, participate in the primary frequency regulation through the droop response of the speed controller, and provide local control of voltage or reactive power flow. These capabilities, and especially the inertial and damping response common to all SMs, are not inherently offered by the power electronics interfaces commonly adopted for the integration of renewable energy sources. A distributed model for production

and local control is also opening the possibility of islanded operation, which is inherently feasible with one or more controllable SMs in the islanded area. Such islanding operation is usually more complex to achieve with power converter interfaces designed for integration with a large-scale power system.

Power from many traditional large-scale generation facilities is currently being replaced by distributed generation capacity from wind power and photovoltaics. The traditional control structures implemented in the power converters for these applications rely on the synchronization to a stable grid frequency supported by large rotating inertias and are not inherently suitable in a SmartGrid context. Thus, from an implementation perspective, significant research efforts are still devoted towards development of control schemes for power electronic converters explicitly conceived to address the conditions emerging in future SmartGrids. Given the inherent benefits of the SMs outlined above, a captivating approach is the control of power electronic converters to replicate the most essential properties of the SM and by that gain equivalent features from a functional point of view. Thus, several alternatives for providing auxiliary services like reactive power control, damping of oscillations and emulation of rotating inertia with power electronic converters have been proposed [3–8]. Some of these control strategies are explicitly designed to mimic the dynamic response of the traditional SM, and can therefore be classified in broad terms as Virtual Synchronous Machines (VSM).

During the last decade, several concepts for VSMs have been presented with different names and different practical implementations [4,8–12]. The first review studies providing an overview of implementations have been recently published in [10,13], with an attempt to define a classification framework presented in [10]. The review in [10] also highlights how some implementations offer only partially the benefits of the SMs while only a few can ensure features as island operation of single or multiple units.

Most previous studies of VSM-based control strategies have presented particular implementation schemes which have been verified by time-domain simulations and/or laboratory experiments. A first study that included detailed modelling and small-signal stability of a particular VSM implementation was presented in [14]. However, this model was mainly developed for tuning of the converter control loops and did not consider the primary power-frequency control or the dynamics of the grid frequency detection needed to ensure an implementation of the VSM damping effect that adapts to variations in the grid frequency. A VSM system model addressing also these issues was recently presented in [15].

This paper includes a comprehensive treatment of a particular VSM implementation, starting from a discussion of the comparative advantages offered by the VSM concept in the context of SmartGrids in abstract terms. Then a brief overview of the VSM development status is offered, with the purpose of identifying general preferences for selecting specific implementations for future SmartGrid applications. The selected implementation is based on an internal representation of the SM inertia and damping behaviour through a reduced order swing equation, together with cascaded voltage and current controllers for operating a Voltage Source Converter (VSC), based on the general scheme from [15]. The paper derives step-by-step a detailed nonlinear mathematical model for this VSM implementation, and a corresponding small signal model in order to apply linear analysis techniques to the system in the perspective of stability assessment and controller tuning. The effect of system parameters on the poles of the linearized system model is also analyzed by calculating the parametric sensitivities of the system eigenvalues. The features and performance of the investigated VSM and its linearized small-signal model is verified with reference to a few selected cases by numerical simulations.

2. Application of Virtual Synchronous Machines in the SmartGrid context

Power generation from distributed renewable energy sources like wind and photovoltaic power plants is usually connected to the power grid through actively controlled power electronic converters, and similar interfaces are applied for energy storage systems and an increasing share of controllable loads. The conventional scheme for such grid connected power converters is based on current controlled Voltage Source Converters (VSCs), which are synchronized to the measured grid voltage through a Phase Locked Loop (PLL) [16]. This approach usually requires a relatively strong grid with the presence of units that can maintain and stabilize the grid frequency and voltage. Even if auxiliary services like frequency and voltage support can be provided by current controlled VSCs, this functionality must be added through additional outer loop controllers which are not inherently applicable for operation in islanded mode [17]. Although this approach can be suitable for a relatively low penetration of grid connected converters, it does not seem sustainable for operation in a long term SmartGrid perspective with the expected dominant presence of power electronic conversion units and a high degree of flexibility in the network configurations.

2.1. Challenges for power converter control in future SmartGrids

In the last decade, several alternative concepts and approaches for control and operation of power converters distributed in the power system have emerged. A noticeable example from the overall system operation point-of-view is the concept of Virtual Power Plants (VPPs) that aims to aggregate generation resources, energy storages and loads into clusters that can be controlled by the distribution system operator in a similar way as traditional power plants [18,19]. Such VPPs should coordinate the controllable units while ensuring supply to the uncontrolled loads in the system, but must also be able to supply auxiliary services like control of voltage or reactive power flow and support the frequency regulation of the system. In small isolated power systems, or in case parts of the distribution system should be able to operate in islanded mode, the generation units aggregated together in one VPP must also ensure a sufficient system inertia to keep the system stable while maintaining the power balance without large frequency deviations. The VPP concepts currently under development are capable of providing frequency-activated power support to the system within a few seconds, and can therefore ensure the steady-state power balance [20]. However, a faster response is required for ensuring an inertia-based power-frequency balance that will be able to keep the system stable in transient conditions. As mentioned, such a power-frequency response is a natural feature of traditional SMs which is not inherently present in the current controlled VSCs usually applied for integrating renewable sources to the grid. SMs offer also additional advantages as automatic synchronization and power sharing in response to changes in the operating conditions.

From these considerations it appears that a SmartGrid can represent a challenging environment for power converter control schemes, especially due to the possible large penetration of power electronics and the variability of the operating conditions. Indeed, a large penetration of converter-interfaced units will correspond to a lower level of physical inertia than in traditional power system dominated by

large synchronous machines, and in certain conditions it can even be necessary to operate pure power electronic, inertia-less, systems. Considering that a flexible SmartGrid framework can result in more frequent reconfigurations of the power system, with corresponding variations in equivalent grid impedance and the possibility to operate parts of the system as groups of electrical islands, the variability of the conditions can introduce a further dimension of complexity. This can also lead to larger and more frequent transients and corresponding requirements for the control systems to maintain individual stable operation as well as contributing to the system stability in a wide range of operating conditions. The design of power electronic control schemes should cope with these challenges and preferably mitigate their effects.

One of the general characteristics of the emerging SmartGrid scenario is the presence of a communication infrastructure that can increase the volume of signal interaction between controllable units in the power system and facilitate their coordination. This can lead to a wide range of options for centralized control schemes, like the mentioned concept of VPPs, where references are determined by a centralized control unit and distributed to the individual converters. However, it should be noted that reducing the necessity of communication between the units, especially during transients, can increase the robustness of the system and reduce the risks in the event of temporary unavailability of the communication infrastructure. Thus, distributed control concepts where individual units can autonomously define their transient response based on local measurements are still relevant. Moreover, decentralized schemes where only steady-state references or set-points are distributed from a centralized system controller can lower the requirements in terms of bandwidth and latencies for the communication infrastructure, resulting in lower installation and operation costs. Multiple examples of possible solutions for decentralized control of power electronic converter can be found in the large literature on isolated MicroGrids [17,21,22] although an exhaustive analysis is beyond the scope of this paper. However, not all of these schemes are suitable for SmartGrid applications where the converter are expected to operate most of the time in grid connected mode. It should also be mentioned that most control schemes that allow for both grid connected and stand-alone operation while also maintaining some decentralized control features, tend to be fairly complicated since transitions between these two modes usually require a reconfiguration of the control structure.

2.2. General characteristics of VSMs

In the emerging SmartGrid context, the VSM concept can offer a basis for realizing flexible decentralized converter control schemes that can operate both in grid connected and islanded conditions, and that can almost seamlessly switch between the corresponding operating modes. Furthermore the inherent inertial characteristic of the VSM can provide services as frequency support and transient power sharing as primary control actions. These are indeed based only on local measurement and do not depend on external communications as in typical alternative schemes. Still, there is no conflict between this local controllability and the ability to operate in a hierarchical structure while following external references and set-points provided by a centralized controller for optimizing the system operation. Moreover, a further advantage of the VSM approach lies in its conceptual simplicity, due to the immediate and intuitive physical interpretation of its behaviour with analogy to the corresponding behaviour of a physical machine.

The dominant behaviour of SMs in terms of inertia response and damping can be modelled by the traditional swing equation [23]. Considering these general characteristics, several control strategies have been developed for allowing power electronic converters to provide synthetic or virtual inertia to the power system, and have been proposed for a variety of applications like for instance wind turbines, energy storage systems and HVDC transmission schemes [3–14,24–26]. Some of these control methods provide a synthetic inertial response to variations in the grid frequency and only a few aims to explicitly replicate the features of the traditional SMs. However, emulation of the inertia and damping effects requires an energy buffer with sufficient capacity to represent the energy storage effect of the emulated rotating inertia available. Thus, the amount of virtual inertia that can be added to the system by a single VSM unit will be limited by the DC-side configuration and by the current rating of the converter.

The current state of the art on the VSM concept has been presented in [10,13]. These reviews identify that some of the implementations proposed as VSMs do not exploit the full potential of the concept because they still rely on a PLL for detecting the grid voltage phase angle, the grid frequency and its derivative, thus requiring the presence of rotating inertia in the grid. Other proposed implementations of the VSM concept are based on the simulation of an internal mathematical SM model inside the control system providing a voltage reference output for the PWM [9]. However, direct open loop PWM signal generation from these voltage references prevents the possibility to explicitly embed the limitations and controlled saturations of voltages and currents that are normally required as protective functions for safe operation of power electronic converters. These protective functions can be easily included in a cascaded control scheme [10,17,27,28] where the output from the VSM inertia emulation is used as reference for a voltage control loop cascaded with an internal current control loop. Numerically, this approach is sufficiently robust for practical implementations and will in the following be assumed as the reference VSM scheme, elaborated from previous studies in [14,15]. It can also be noted that the implementation of a VSM based on the swing equation providing references for operation of the converter, under certain conditions has been shown to be equivalent to the frequency-droop-based control strategies first developed for Uninterruptable Power Supply (UPS) systems and MicroGrids, as demonstrated in [10,29]. However, the interpretation of the parameters in a VSM approach seems to be simpler and more intuitive than the equivalent parameters in the commonly applied MicroGrid schemes and, thus, preferable.

3. Mathematical model of the VSM reference implementation

This section describes the control scheme for the selected VSM reference implementation, considering each functional block, and derives the corresponding mathematical model.

3.1. Control system overview

An overview of the studied VSM configuration is shown in Fig. 1, where a VSC is connected to a grid through an LC filter. In the following, the switching effects of the VSC are neglected and an ideal average model is assumed for modelling the converter. Furthermore, no application-specific constraints of the DC-side of the VSC are considered and, thus, modelling and control of the energy source or storage on the DC side of the converter is not further discussed.
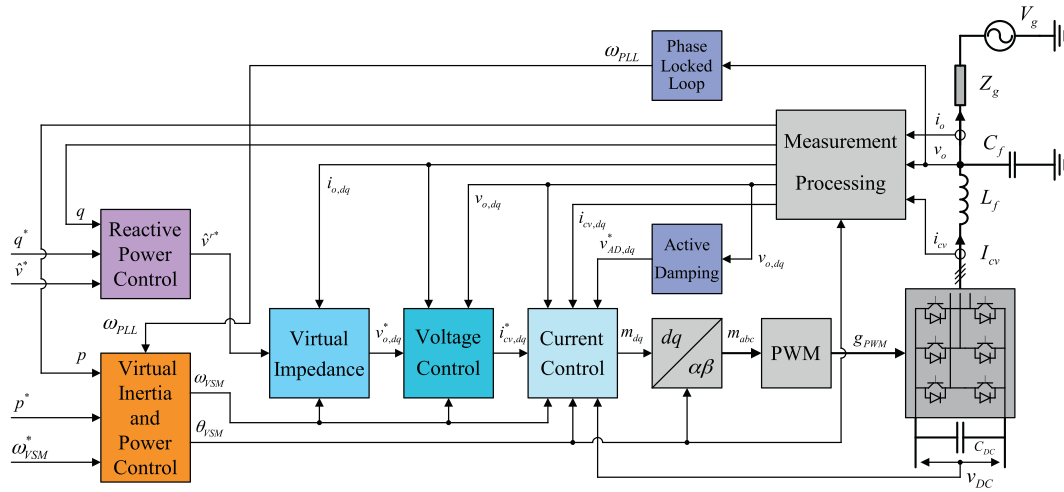
Fig. 1. Overview of investigated system configuration and control structure for the Virtual Synchronous Machine.

The VSM-based power control with virtual inertia provides frequency and phase angle references ω_{VSM} and θ_{VSM} to the internal control loops for operating the VSC, while a reactive power controller provides the voltage amplitude reference $\hat{v}^{r*}$. Thus, the VSM inertia emulation and the reactive power controller appear as outer loops providing the references for the cascaded voltage and current controllers. A PLL detects the actual grid frequency, but this frequency is only used for implementing the damping term in the swing equation. Thus, the operation of the inner loop controllers does not rely on the PLL as in conventional VSC control systems, but only on the power-balance-based synchronization mechanism of the VSM inertia.

3.2. Modelling conventions

In Fig. 1, upper case symbols represent physical values of the electrical circuit. The control system implementation and the modelling of the system are based on per unit quantities, denoted by lower case letters where the base values are defined from the apparent power rating and the rated peak value of the phase voltage [30].

The modelling, analysis and control of the electrical system is implemented in Synchronous Reference Frames (SRFs). The transformation from the stationary reference frame into the SRFs are based on the amplitude-invariant Park transformation, with the d-axis aligned with a voltage vector and the q-axis leading the d-axis by 90° [30]. Thus, the magnitude of current and voltage vectors at rated conditions is 1.0 pu.

Whenever possible, SRF equations are presented in complex space vector notation as:

$$\mathbf{x} = x_d + j \cdot x_q \tag{1}$$

Thus, active and reactive powers can be expressed on complex or scalar form as:

$$p = Re(\mathbf{v} \cdot \breve{\mathbf{i}}) = v_d \cdot i_d + v_q \cdot i_q$$
$$q = Im(\mathbf{v} \cdot \breve{\mathbf{i}}) = -v_d \cdot i_q + v_q \cdot i_d \tag{2}$$

The current directions indicated in Fig. 1 result in positive values for active and reactive powers flowing from the converter into the grid.

3.3. System modelling

In the following sub-sections, the implementation of each functional block of the VSM-based control and the mathematical models of all system elements from Fig. 1 are presented as a basis for developing a non-linear model of the system. This system model will also be used to establish a linearized small-signal state-space representation.

3.3.1. VSM inertia emulation and active power droop control

The emulation of a rotating inertia and the power-balance based synchronization mechanisms of this virtual inertia is the main difference between the investigated VSM control structure and conventional control systems for VSCs. The VSM implementation investigated in this case is based on a conventional swing equation representing the inertia and damping of a traditional SM [10,14]. The swing equation used for the implementation is linearized with respect to the speed so that the acceleration of the inertia is determined by the power balance according to:

$$\frac{d\omega_{VSM}}{dt} = \frac{p^{r*}}{T_a} - \frac{p}{T_a} - \frac{p_d}{T_a} \tag{3}$$

In this equation, p^{r*} is the virtual mechanical input power, p is the measured electrical power flowing from the VSM into the grid, and p_d is the damping power, while the mechanical time constant is defined as T_a (corresponding to $2H$ in a traditional SM). The per unit mechanical speed ω_{VSM} of the virtual inertia is then given by the integral of the power balance while the corresponding phase angle θ_{VSM} is given by the integral of the speed. A block diagram showing the implementation of the VSM swing equation is shown on the right in Fig. 2.
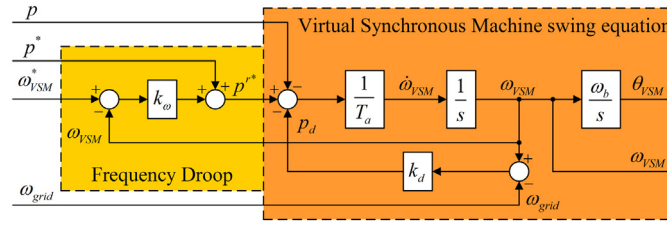
Fig. 2. Virtual Synchronous Machine inertia emulation with power-frequency droop.

The VSM damping power p_d, representing the damping effect of a traditional SM, is defined by the damping constant k_d and the difference between the VSM speed and the actual grid frequency. Thus, an estimate of the actual grid frequency is needed for the VSM implementation. As indicated in the figure, the frequency estimate is in this case labelled as ω_{PLL} and is provided by a PLL.

An external frequency droop, equivalent to the steady-state characteristics of the speed governor for a traditional synchronous machine, is included in the power control of the VSM as shown in the left part of Fig. 2. This power-frequency droop is characterized by the droop constant k_ω acting on the difference between a frequency reference ω_{VSM}^* and the actual VSM speed ω_{VSM}. Thus, the virtual mechanical input power p^{r*} to the VSM swing equation is given by the sum of the external power reference set-point, p^*, and the frequency droop effect, as shown on the left of Fig. 2.

For modelling the VSM in a SRF, the phase angle of the VSM in grid connected mode should be constant under steady-state conditions and should correspond to the phase displacement between the virtual position of the VSM internal voltage and the position of the grid voltage vector. Since only the deviation of the VSM speed from the actual grid frequency should be modelled to achieve this, a new set of variables representing the speed deviation $\delta\omega_{VSM}$ and the corresponding phase angle difference $\delta\theta_{VSM}$ is introduced. Thus, the power balance of the VSM inertia can be expressed by (4), while the VSM phase displacement is defined by (5):

$$\frac{d\delta\omega_{VSM}}{dt} = \frac{p^*}{T_a} - \frac{p}{T_a} - \frac{k_d(\omega_{VSM} - \omega_{PLL})}{T_a} - \frac{k_\omega(\omega_{VSM} - \omega^*)}{T_a} \tag{4}$$

$$\frac{d\delta\theta_{VSM}}{dt} = \delta\omega_{VSM} \cdot \omega_b \tag{5}$$

Since the VSM speed in steady state will become equal to the grid frequency ω_g, the frequency deviation $\delta\omega_{VSM}$ will return to zero under stable grid connected operation.

The actual per unit speed of the VSM shown in the block diagram of Fig. 2 can be expressed from the speed deviation $\delta\omega_{VSM}$ resulting from (4) and the grid frequency ω_g as given by (6). The corresponding VSM phase angle θ_{VSM} is then defined by (7)

$$\omega_{VSM} = \delta\omega_{VSM} + \omega_g \tag{6}$$

$$\frac{d\theta_{VSM}}{dt} = \omega_{VSM} \cdot \omega_b \tag{7}$$

The phase angle θ_{VSM} will then become a saw-tooth signal between 0 and 2π, which is the phase angle that will be used for the transformation between the rotating reference frame defined by the VSM inertia and the three-phase signals, as indicated in Fig. 1.

3.3.2. Reactive power droop controller

The droop-based reactive power controller applied in this case is similar to the controllers commonly applied in microgrid systems [17,27]. The voltage amplitude reference $\hat{v}^{r*}$ used for the inner loop voltage and current control is then calculated by (8) where $\hat{v}^*$ is the external voltage amplitude reference and q^* is the reactive power reference. The gain k_q is the reactive power droop gain acting on the difference between the reactive power reference and the filtered reactive power measurement q_m. The state of the corresponding first order low pass filter applied in this case is defined by (9), where ω_f is the cut-off frequency. A block diagram of the resulting control structure is shown in Fig. 3:

$$\hat{v}^{r*} = \hat{v}^* + k_q(q^* - q_m) \tag{8}$$

$$\frac{dq_m}{dt} = -\omega_f \cdot q_m + \omega_f \cdot q \tag{9}$$

3.3.3. Reference frame orientations

The synchronization of the VSM control system to the grid is based on the phase angle orientation of the virtual rotor of the VSM, and the phase angle θ_{VSM} is used in the transformations between the stationary reference frame and the VSM-oriented SRF. Thus, the power
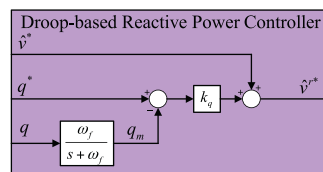

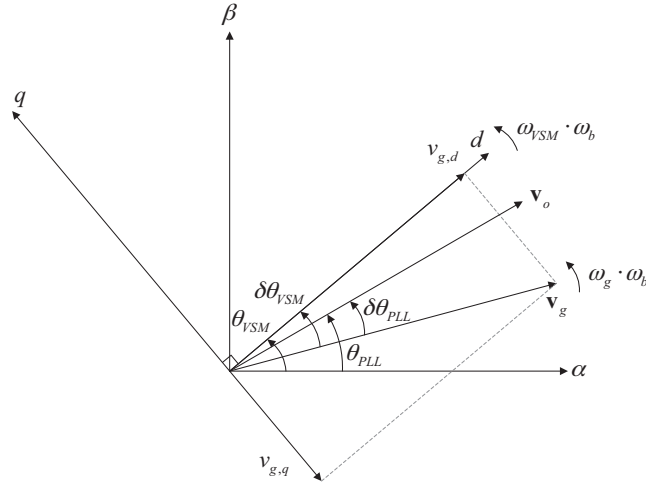**Fig. 3.** Reactive power droop controller.

Fig. 4. Vector diagram defining the SRF and voltage vector orientations.

balance of the VSM swing equation will ensure the synchronization to the grid voltage without the need for a traditional PLL. Since the VSM-oriented SRF in steady state rotates with the same frequency as the grid voltage, this phase angle will be continuously increasing between 0 and 2π, as indicated in the vector diagram shown in Fig. 4. According to its definition, the phase angle $\delta\theta_{VSM}$ is instead representing the phase difference between the VSM SRF orientation and the rotating grid voltage vector, as also indicated in Fig. 4.

The VSM-oriented SRF is used for both control and modelling of the system, and therefore, also the model of the electrical system will be represented in this reference frame. This has significant advantages for the modelling of the system, since multiple reference frame transformations between a local SRF for controller implementation and a global SRF for electrical system modelling can be avoided. Considering the amplitude of the equivalent grid voltage $\hat{v}_g$ to be known, the voltage vector $\mathbf{v}_g$ in the VSM-oriented SRF can then be expressed by (10):

$$\mathbf{v}_g = \hat{v}_g e^{-j\delta\theta_{VSM}} \tag{10}$$

By the power-balance-based synchronization effect of the VSM swing equation, the control system defines its own reference frame orientation with respect to the grid voltage. In principle, no additional reference frames are needed to model the system from Fig. 1. However, since an estimate for the grid frequency is used to implement the VSM damping effect, a PLL operating on the measured voltage $\mathbf{v}_o$ at the filter capacitors is implemented as part of the control system. Thus, this PLL will establish its own SRF aligned with the voltage vector $\mathbf{v}_o$. The phase angle displacement of this PLL with respect to the grid voltage can then be defined as $\delta\theta_{PLL}$ in a similar way as for the phase angle displacement of the VSM. The detailed implementation of the PLL will be presented in the following sub-section, but the definition of its steady state phase displacement $\delta\theta_{PLL}$ with respect to the grid voltage, and the corresponding phase angle θ_{PLL} between the rotating PLL-oriented SRF and the stationary reference frame, is shown in Fig. 4.

According to the definitions indicated in Fig. 4, the phase angle between the VSM and PLL oriented SRFs will be defined by the difference between the VSM and PLL angles. For modelling of the PLL in its own reference frame, the voltage $\mathbf{v}_o$ at the filter capacitors can be transformed from the VSM-oriented reference frame to the PLL-oriented reference frame by:

$$\mathbf{v}_o^{PLL} = \mathbf{v}_o^{VSM} e^{-j(\delta\theta_{PLL} - \delta\theta_{VSM})} \tag{11}$$

3.3.4. Phase locked loop

The Phase Locked Loop (PLL) applied in this case for tracking of the actual grid frequency is based on [31,32] and its structure is shown in Fig. 5. This PLL is using first order low-pass filters on the estimated d- and q-axis voltage components and an inverse tangent function to calculate the phase angle error of the PLL. This phase angle error e_{PLL} is the input to a PI controller tracking the frequency of the measured voltage. For the practical implementation, the estimated frequency ω_{PLL} is then integrated to obtain the estimate of the actual instantaneous phase angle θ_{PLL} used for transformation of the voltage measurements into the PLL-oriented SRF. For modelling of the PLL, the voltage vector $\mathbf{v}_o$ in the VSM-oriented SRF must be transformed into the PLL-oriented SRF according to (11).
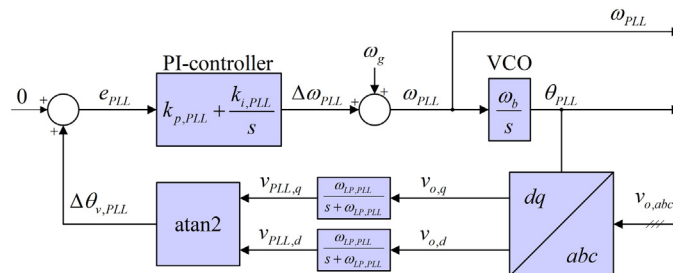

Fig. 5. Phase locked loop.

The states of the applied first order low-pass filters in the PLL, defining the filtered voltage $\mathbf{v}_{PLL}$, can be expressed by (12), where the cut-off frequency of the applied low pass filters is given by $\omega_{LP,PLL}$:

$$\frac{d\mathbf{v}_{PLL}}{dt} = -\omega_{LP,PLL} \cdot \mathbf{v}_{PLL} + \omega_{LP,PLL} \cdot \mathbf{v}_o e^{-j(\delta\theta_{PLL}-\delta\theta_{VSM})} \tag{12}$$

The integrator state ε_{PLL} of the PI controller can then be defined by:

$$\frac{d\varepsilon_{PLL}}{dt} = \tan^{-1}\left(\frac{V_{PLL,q}}{V_{PLL,d}}\right) \tag{13}$$

In the same way as explained for the SRF modelling of the VSM swing equation, a speed deviation $\delta\omega_{PLL}$ with respect to the grid frequency is defined for the PLL according to (14). The corresponding phase angle displacement, $\delta\theta_{PLL}$, of the PLL is then defined by (15):

$$\delta\omega_{PLL} = k_{p,PLL} \cdot \tan^{-1}\left(\frac{V_{PLL,q}}{V_{PLL,d}}\right) + k_{i,PLL} \cdot \varepsilon_{PLL} \tag{14}$$

$$\frac{d\delta\theta_{PLL}}{dt} = \delta\omega_{PLL} \cdot \omega_b \tag{15}$$

In accordance with the definitions introduced for the VSM swing equation, the actual per unit frequency ω_{PLL} detected by the PLL is given by (16). The phase angle used in the implementation of the PLL, for transformation of the measured three-phase voltage measurements into the PLL-oriented SRF, is then defined by θ_{PLL} according to (17):

$$\omega_{PLL} = \delta\omega_{PLL} + \omega_g \tag{16}$$

$$\frac{d\theta_{PLL}}{dt} = \omega_{PLL} \cdot \omega_b \tag{17}$$

3.3.5. Virtual impedance and voltage controllers

As indicated in Fig. 1, the voltage amplitude reference $\hat{v}^{r*}$ resulting from the reactive power droop controller in Fig. 3 is passed through a virtual impedance before it is used as a reference for controlling the voltage $\mathbf{v}_o$ at the filter capacitors. This virtual impedance can be considered as an emulation of the quasi-stationary characteristics of the synchronous impedance in a traditional SM. The virtual impedance will influence the steady-state and dynamic operation of the VSM, and it will be shown how it can be used to shape the dynamic characteristics of the system. Since power flowing through the virtual inductance will cause a phase angle displacement between the grid voltage and the virtual inertia position of the VSM, it will also reduce the sensitivity of the VSM to small disturbances in the grid. The influence from the virtual resistance r_v and inductance l_v on the capacitor voltage reference vector $\mathbf{v}_o^*$ is defined on basis of the current $\mathbf{i}_o$ according to [33,34]:

$$\mathbf{v}_o^* = \hat{v}^{r*} - (r_v + j \cdot \omega_{VSM} \cdot l_v) \cdot \mathbf{i}_o \tag{18}$$

The resulting d- and q-axis voltage components $v_{o,d}^*$ and $v_{o,q}^*$ are used directly as references for the decoupled SRF PI voltage controllers as shown in the left part of Fig. 6.

The detailed structure of the SRF PI controllers for the filter capacitor voltage is shown in the middle of Fig. 6, and is producing the reference values $\mathbf{i}_{cv}^*$ for the converter currents [27]. These current references can be expressed by (19), where the PI controller gains are defined by k_{pv} and k_{iv}. A gain factor k_{ffi} that can be set to 1 or 0 is used to enable or disable the feed-forward of measured currents flowing into the grid. It should also be noted that the decoupling terms of the voltage controller are based on the per unit speed of the VSM inertia as defined in (6). The states $\boldsymbol{\xi}$ are defined to represent the integrators of the PI voltage controllers as given by (20):

$$\mathbf{i}_{cv}^* = k_{pv}(\mathbf{v}_o^* - \mathbf{v}_o) + k_{iv}\boldsymbol{\xi} + j \cdot c_1 \cdot \omega_{VSM} \cdot \mathbf{v}_o + k_{ffi} \cdot i_o \tag{19}$$

$$\frac{d\boldsymbol{\xi}}{d} = \mathbf{v}_o^* - \mathbf{v}_o \tag{20}$$

The current references from the voltage controllers should be limited to avoid over-currents in case of voltage drops, fault conditions or other severe transients. This also implies that the voltage controllers must be protected from windup conditions in case the current references are saturated. However, the required limitations and anti-windup techniques for the investigated VSM scheme are similar to what is needed in conventional droop-based control schemes with cascaded SRF voltage and current controllers, as for instance discussed in [28]. Since these limitations are not influencing the dynamics of the control scheme within the normal operating range, further details will not be discussed here.

3.3.6. Current controllers and active damping

The applied inner loop current controllers are conventional SRF PI controllers with decoupling terms [27,35], as shown in the right side part of Fig. 6. The output voltage reference from the controller is defined by (21), where the resulting voltage reference for the converter is denoted by $\mathbf{v}_{cv}^*$. The proportional and integral gains of the PI controller are defined by k_{pc} and k_{ic}, and a gain factor k_{ffv} is used to disable or enable the voltage feed-forward in the output of the current controllers. The states $\boldsymbol{\gamma}$ are defined to represent the integrators of the PI controllers according to (22):

$$\mathbf{v}_{cv}^* = k_{pc}(\mathbf{i}_{cv}^* - \mathbf{i}_{cv}) + k_{ic} \cdot \boldsymbol{\gamma} + j \cdot l_1 \cdot \omega_{VSM} \cdot \mathbf{i}_{cv} + k_{ffv} \cdot \mathbf{v}_o - \mathbf{v}_{AD}^* \tag{21}$$

$$\frac{d\boldsymbol{\gamma}}{dt} = \mathbf{i}_{cv}^* - \mathbf{i}_{cv} \tag{22}$$

In (21), the voltage reference for the converter also includes an active damping term $\mathbf{v}_{AD}^*$ designed for suppressing LC oscillations in the filter [36]. The implementation of the active damping algorithm is shown in Fig. 7, and is based on high pass filtering of the measured voltage $\mathbf{v}_o$, obtained from the difference between $\mathbf{v}_o$ and the low pass filtered value of the same voltage. The resulting high pass filtered signal is then scaled by the gain k_{AD} according to (23) and subtracted from the output of the current controllers to cancel detected oscillations in the capacitor voltages:

$$\mathbf{v}_{AD}^* = k_{AD}(\mathbf{v}_o - \boldsymbol{\varphi}) \tag{23}$$

The corresponding internal states $\boldsymbol{\varphi}$ of the low pass filters used for the active damping are defined by (24), where ω_{AD} is the cut-off frequency:

$$\frac{d\boldsymbol{\varphi}}{dt} = \omega_{AD} \cdot \mathbf{v}_o - \omega_{AD} \cdot \boldsymbol{\varphi} \tag{24}$$

For the practical implementation of the VSC control system, the voltage reference $\mathbf{v}_{cv}^*$ resulting from the current controller and the active damping is divided by the measured DC-link voltage to result in the modulation index $\mathbf{m}$ as shown to the right of Fig. 6. Neglecting the switching operation of the converter and any delay due to the PWM implementation, the instantaneous average value of the per unit converter output voltage is given by the product of the modulation index and the actual DC-voltage. Under this assumption, the output converter voltage will be approximately equal to the voltage reference as summarized by (25) [37]:

$$\mathbf{m} = \frac{\mathbf{v}_{cv}^*}{v_{DC}}, \quad \mathbf{v}_{cv} = \mathbf{m} \cdot v_{DC} \rightarrow \mathbf{v}_{cv} \approx \mathbf{v}_{cv}^* \tag{25}$$

Thus, the AC side operation of the converter will be effectively decoupled from any dynamics in the DC voltage, and it is not necessary to further discuss or model the DC side of the converter for achieving an accurate representation of the dynamics on the AC side. It should be noted that the actual source or storage unit connected to the DC link of the converter might still impose restrictions on the allowable power exchange during various operating conditions. However, to maintain generality and avoid detailed discussion of particular application-specific limitations it will be assumed that the power requested from the AC side is always available at the DC link of the converter.

3.3.7. Electrical system equations

The electrical system included in the model according to Fig. 1 consists of a set of filter inductors connected to the converter, a shunt capacitor bank representing the capacitance of the LC filter, and a Thévenin equivalent of the grid. This simple structure is assumed to achieve a simple model that mainly includes the dynamics of the converter control system and its interaction with the equivalent grid voltage. However, a more complex AC grid topology can be easily included in the model for both simulations and analysis. Considering an instantaneous average model of the converter, the SRF state space equations of the electrical system can be established as given by (26) [27,35]:

$$\begin{aligned}
\frac{d\mathbf{i}_{cv}}{dt} &= \frac{\omega_b}{l_f}\mathbf{v}_{cv} - \frac{\omega_b}{l_f}\mathbf{v}_o - \left(\frac{r_{l_f}\omega_b}{l_f} + j \cdot \omega_g\omega_b\right)\mathbf{i}_{cv} \\
\frac{d\mathbf{v}_o}{dt} &= \frac{\omega_b}{c_f}\mathbf{i}_{cv} - \frac{\omega_b}{c_f}\mathbf{i}_g - j \cdot \omega_g\omega_b \cdot \mathbf{v}_o \\
\frac{d\mathbf{i}_o}{dt} &= \frac{\omega_b}{l_g}\mathbf{v}_o - \frac{\omega_b}{l_g}\mathbf{v}_g - \left(\frac{r_g\omega_b}{l_g} + j \cdot \omega_g\omega_b\right)\mathbf{i}_o
\end{aligned} \tag{26}$$

In these equations $\mathbf{i}_{cv}$ is the filter inductor current, $\mathbf{v}_{cv}$ is the converter output voltage, $\mathbf{v}_o$ is the voltage at the filter capacitors, $\mathbf{i}_g$ is the current flowing into the grid equivalent and $\mathbf{v}_g$ is the grid equivalent voltage. The inductance and equivalent resistance of the filter inductor is given by l_f and r_{lf}, the filter capacitor is c_f, while the grid inductance and resistance are given by l_g and r_g. The per unit grid frequency is given by ω_g, while the base angular grid frequency is defined by ω_b. It should be noted that the state space model from (26) can represent the electrical system in any SRF, but in this case the system will always be modelled in the SRF defined by the VSM swing equation.

It should also be noted that the presented model only represents the case of grid-connected operation, while the investigated VSM scheme is inherently suitable for stand-alone operation. In this case the operational frequency will only be determined by the actual load in the system, the power-frequency droop gain and the power and frequency references for the VSM. Further details on modelling of the investigated VSM implementation in islanded operation, and corresponding analysis of the dynamic characteristics in stand-alone mode can be found in [38].

3.4. Non-linear system model in grid-connected operation

All equations needed for detailed modelling of the VSM configuration in grid-connected operation have been presented in the previous sub-sections, and can be reduced to a model on state-space form with 19 distinct state variables and 6 input signals, with the state vector $\mathbf{x}$ and the input vector $\mathbf{u}$ defined by (27). The resulting non-linear state-space model of the overall system is given by (28):

$$\begin{aligned}
\mathbf{x} &= \begin{bmatrix} v_{o,d} & v_{o,q} & i_{cv,d} & i_{cv,q} & \gamma_d & \gamma_q & i_{o,d} & i_{o,q} & \varphi_d & \varphi_q \cdots \\ \cdots v_{PLL,d} & v_{PLL,q} & \varepsilon_{PLL} & \delta\theta_{VSM} & \xi_d & \xi_q & q_m & \delta\omega_{VSM} & \delta\theta_{PLL} \end{bmatrix}^T \\
\mathbf{u} &= \begin{bmatrix} p^* & q^* & \hat{v}_g & \hat{v}^* & \omega^* & \omega_g \end{bmatrix}^T
\end{aligned} \tag{27}$$

$$\frac{dv_{o,d}}{dt} = \omega_b \omega_g v_{o,q} + \frac{\omega_b}{c_f} i_{cv,d} - \frac{\omega_b}{c_f} i_{o,d}$$

$$\frac{dv_{o,q}}{dt} = -\omega_b \omega_g v_{o,d} + \frac{\omega_b}{c_f} i_{cv,q} - \frac{\omega_b}{c_f} i_{o,q}$$

$$\frac{di_{cv,d}}{dt} = \frac{\omega_b(k_{ffv} - 1 - k_{AD} - k_{pc}k_{pv})}{l_f} v_{o,d} - \frac{\omega_b c_f k_{pc}}{l_f} \omega_g v_{o,q} - \frac{\omega_b(k_{pc}+r_f)}{l_f} i_{cv,d} + \frac{\omega_b k_{ic}}{l_f} \gamma_d + \frac{\omega_b k_{pc}(k_{ffi}-k_{pv}r_v)}{l_f} i_{o,d} + \frac{\omega_b k_{pc}k_{pv}l_v}{l_f} \omega_g i_{o,q}$$

$$+ \frac{\omega_b k_{AD}}{l_f} \varphi_d + \frac{\omega_b k_{iv}k_{pc}}{l_f} \xi_d - \frac{\omega_b k_{pc}k_{pv}k_q}{l_f} q_m - \omega_b i_{cv,q}\delta\omega_{VSM} + \frac{\omega_b k_{pc}k_{pv}l_v}{l_f} i_{o,q}\delta\omega_{VSM} - \frac{\omega_b c_f k_{pc}}{l_f} v_{o,q}\delta\omega_{VSM} + \frac{\omega_b k_{pc}k_{pv}k_q}{l_f} q^* + \frac{\omega_b k_{pc}k_{pv}}{l_f} \hat{v}^*$$

$$\frac{di_{cv,q}}{dt} = \frac{\omega_b c_f k_{pc}}{l_f} \omega_g v_{o,d} + \frac{\omega_b(k_{ffv} - 1 - k_{AD} - k_{pc}k_{pv})}{l_f} v_{o,q} - \frac{\omega_b(k_{pc}+r_f)}{l_f} i_{cv,q} + \frac{\omega_b k_{ic}}{l_f} \gamma_q - \frac{\omega_b k_{pc}k_{pv}l_v}{l_f} \omega_g i_{o,d} + \frac{\omega_b k_{pc}(k_{ffi}-k_{pv}r_v)}{l_f} i_{o,q}$$

$$+ \frac{\omega_b k_{AD}}{l_f} \varphi_q + \frac{\omega_b k_{iv}k_{pc}}{l_f} \xi_q + \omega_b i_{cv,d}\delta\omega_{VSM} - \frac{\omega_b k_{pc}k_{pv}l_v}{l_f} i_{o,d}\delta\omega_{VSM} + \frac{\omega_b c_f k_{pc}}{l_f} v_{o,d}\delta\omega_{VSM}$$

$$\frac{d\gamma_d}{dt} = -k_{pv}v_{o,d} - c_f \omega_g v_{o,q} - i_{cv,d} + (k_{ffi} - k_{pv}r_v)i_{o,d} + k_{pv}l_v\omega_g i_{o,q} + k_{iv}\xi_d - k_{pv}k_q q_m + k_{pv}l_v i_{o,q}\delta\omega_{VSM} - c_f v_{o,q}\delta\omega_{VSM} + k_{pv}k_q q^* + k_{pv}\hat{v}^*$$

$$\frac{d\gamma_d}{dt} = c_f \omega_g v_{o,d} - k_{pv}v_{o,q} - i_{cv,q} - k_{pv}l_v\omega_g i_{o,d} + (k_{ffi} - k_{pv}r_v)i_{o,q} + k_{iv}\xi_q - k_{pv}l_v i_{o,d}\delta\omega_{VSM} + c_f v_{o,d}\delta\omega_{VSM}$$

$$\frac{di_{o,d}}{dt} = \frac{\omega_b}{l_g} v_{o,d} - \frac{\omega_b r_g}{l_g} i_{o,d} + \omega_b \omega_g i_{o,q} + \frac{\omega_b \hat{v}_g \cos(\delta\theta_{VSM})}{l_g}$$

$$\frac{di_{o,q}}{dt} = \frac{\omega_b}{l_g} v_{o,q} - \omega_b \omega_g i_{o,d} - \frac{\omega_b r_g}{l_g} i_{o,q} + \frac{\omega_b \hat{v}_g \sin(\delta\theta_{VSM})}{l_g}$$

$$\frac{d\varphi_d}{dt} = \omega_{AD} v_{o,d} - \omega_{AD}\varphi_d$$

$$\frac{d\varphi_q}{dt} = \omega_{AD} v_{o,q} - \omega_{AD}\varphi_q$$

$$\frac{dv_{PLL,d}}{dt} = \omega_{LP,PLL}v_{o,d}\cos(\delta\theta_{PLL} - \delta\theta_{VSM}) + \omega_{LP,PLL}v_{o,q}\sin(\delta\theta_{PLL} - \delta\theta_{VSM}) - \omega_{LP,PLL}v_{PLL,d}$$

$$\frac{dv_{PLL,q}}{dt} = -\omega_{LP,PLL}v_{o,d}\sin(\delta\theta_{PLL} - \delta\theta_{VSM}) + \omega_{LP,PLL}v_{o,q}\cos(\delta\theta_{PLL} - \delta\theta_{VSM}) - \omega_{LP,PLL}v_{PLL,q}$$

$$\frac{d\varepsilon_{PLL}}{dt} = \tan^{-1}\left(\frac{v_{PLL,q}}{v_{PLL,d}}\right)$$

$$\frac{d\delta\theta_{VSM}}{dt} = \omega_b \delta\omega_{VSM}$$

$$\frac{d\delta\xi_d}{dt} = -v_{o,d} - r_v i_{o,d} + l_v\omega_g i_{o,q} - k_q q_m + l_v i_{o,q}\delta\omega_{VSM} + k_q q^* + \hat{v}^*$$

$$\frac{d\delta\xi_q}{dt} = -v_{o,q} - l_v\omega_g i_{o,d} - r_v i_{o,q} - l_v i_{o,d}\delta\omega_{VSM}$$

$$\frac{dq_m}{dt} = -\omega_f i_{o,q}v_{o,d} + \omega_f i_{o,d}v_{o,q} - \omega_f q_m$$

$$\frac{d\delta\omega_{VSM}}{dt} = -\frac{1}{T_a} i_{o,d}v_{o,d} - \frac{1}{T_a} i_{o,q}v_{o,q} + \frac{k_d k_{p,PLL}}{T_a}\tan^{-1}\left(\frac{v_{PLL,q}}{v_{PLL,d}}\right) + \frac{k_d k_{i,PLL}}{T_a}\varepsilon_{PLL} - \frac{k_d + k_\omega}{T_a}\delta\omega_{VSM} + \frac{1}{T_a}p^* + \frac{k_\omega}{T_a}\omega^* - \frac{k_\omega}{T_a}\omega_g$$

$$\frac{d\delta\theta_{PLL}}{dt} = \omega_b k_{p,PLL}\tan^{-1}\left(\frac{v_{PLL,q}}{v_{PLL,d}}\right) + \omega_b k_{i,PLL}\varepsilon_{PLL}$$

$$(28)$$

The steady state operating point of the system under any combinations of input signals can be found by solving this nonlinear system model with derivative terms set to zero.

3.5. Small signal model of the reference VSM

Since the state-space model from (28) is nonlinear, classical stability assessment techniques based on eigenvalues are not directly applicable. Thus, in this section, a corresponding linearized small-signal state-space model is derived in the form given by:

$$\Delta\dot{\mathbf{x}} = \mathbf{A}\cdot\Delta\mathbf{x} + \mathbf{B}\cdot\Delta\mathbf{u}. \tag{29}$$

where the prefix Δ denotes small-signal deviations around the steady-state operating point [30]. The values of the state variables at this linearization point are denoted by subscript '0' when they appear in the matrices. For convenience of notation, the dynamic matrix A is expressed through four sub-matrices according to:

$$\begin{bmatrix} \Delta\dot{\mathbf{x}}_1 \\ \Delta\dot{\mathbf{x}}_2 \end{bmatrix} = \begin{bmatrix} \mathbf{A}_{11} & \mathbf{A}_{12} \\ \mathbf{A}_{21} & \mathbf{A}_{22} \end{bmatrix} \cdot \begin{bmatrix} \Delta\mathbf{x}_1 \\ \Delta\mathbf{x}_2 \end{bmatrix} + \mathbf{B}\cdot\Delta\mathbf{u} \tag{30}$$

where $\mathbf{A}_{11}$, $\mathbf{A}_{12}$, $\mathbf{A}_{13}$ and $\mathbf{A}_{22}$ are given by (31)–(34), while the $\mathbf{B}$ matrix is given by (35):

$$\mathbf{A}_{11} = \begin{bmatrix}
0 & \omega_b\omega_{g,0} & \frac{\omega_b}{c_f} & 0 & 0 & 0 & -\frac{\omega_b}{c_f} & 0 & 0 & 0 \\
-\omega_b\omega_{g,0} & 0 & 0 & \frac{\omega_b}{c_f} & 0 & 0 & 0 & -\frac{\omega_b}{c_f} & 0 & 0 \\
\frac{\omega_b(k_{ffv}-1-k_{AD}-k_{pc}k_{pv})}{l_f} & -\frac{\omega_b c_f k_{pc}\omega_{g,0}}{l_f} & -\frac{\omega_b(k_{pc}+r_f)}{l_f} & 0 & \frac{\omega_b k_{ic}}{l_f} & 0 & \frac{\omega_b k_{pc}(k_{ffi}-k_{pv}r_v)}{l_f} & \frac{\omega_b k_{pc}k_{pv}l_v\omega_{g,0}}{l_f} & \frac{\omega_b k_{AD}}{l_f} & 0 \\
\frac{\omega_b c_f k_{pc}\omega_{g,0}}{l_f} & \frac{\omega_b(k_{ffv}-1-k_{AD}-k_{pc}k_{pv})}{l_f} & 0 & -\frac{\omega_b(k_{pc}+r_f)}{l_f} & 0 & \frac{\omega_b k_{ic}}{l_f} & -\frac{\omega_b\omega_g k_{pc}k_{pv}l_v}{l_f} & \frac{\omega_b k_{pc}(k_{ffi}-k_{pv}r_v)}{l_f} & 0 & \frac{\omega_b k_{AD}}{l_f} \\
-k_{pv} & -c_f\omega_{g,0} & -1 & 0 & 0 & 0 & k_{ffi}-k_{pv}r_v & k_{pv}l_v\omega_{g,0} & 0 & 0 \\
c_f\omega_{g,0} & -k_{pv} & 0 & -1 & 0 & 0 & -k_{pv}l_v\omega_{g,0} & k_{ffi}-k_{pv}r_v & 0 & 0 \\
\frac{\omega_b}{l_g} & 0 & 0 & 0 & 0 & 0 & -\frac{\omega_b r_g}{l_g} & \omega_b\omega_{g,0} & 0 & 0 \\
0 & \frac{\omega_b}{l_g} & 0 & 0 & 0 & 0 & -\omega_b\omega_{g,0} & -\frac{\omega_b r_g}{l_g} & 0 & 0 \\
\omega_{AD} & 0 & 0 & 0 & 0 & 0 & 0 & 0 & -\omega_{AD} & 0 \\
0 & \omega_{AD} & 0 & 0 & 0 & 0 & 0 & 0 & 0 & -\omega_{AD}
\end{bmatrix} \quad (31)$$

$$\mathbf{A}_{12} = \begin{bmatrix}
0 & 0 & 0 & 0 & 0 & 0 & 0 & 0 \\
0 & 0 & 0 & 0 & 0 & 0 & 0 & 0 \\
0 & 0 & 0 & 0 & \frac{\omega_b k_{iv}k_{pc}}{l_f} & 0 & -\frac{\omega_b k_{pc}k_{pv}k_q}{l_f} & \frac{\omega_b(-l_f i_{cv,q,0}+k_{pc}k_{pv}l_v i_{o,q,0}-c_f k_{pc}v_{o,q,0})}{l_f} & 0 \\
0 & 0 & 0 & 0 & 0 & \frac{\omega_b k_{iv}k_{pc}}{l_f} & 0 & \frac{\omega_b(l_f i_{cv,d,0}-k_{pc}k_{pv}l_v i_{o,d,0}+c_f k_{pc}v_{o,d,0})}{l_f} & 0 \\
0 & 0 & 0 & 0 & k_{iv} & 0 & -k_{pv}k_q & k_{pv}l_v i_{o,q,0}-c_f v_{o,q,0} & 0 \\
0 & 0 & 0 & 0 & 0 & k_{iv} & 0 & -k_{pv}l_v i_{o,d,0}+c_f v_{o,d,0} & 0 \\
0 & 0 & 0 & \frac{\omega_b\hat{v}_{g,0}\sin(\delta\theta_{VSM,0})}{l_g} & 0 & 0 & 0 & 0 & 0 \\
0 & 0 & 0 & \frac{\omega_b\hat{v}_{g,0}\cos(\delta\theta_{VSM,0})}{l_g} & 0 & 0 & 0 & 0 & 0 \\
0 & 0 & 0 & 0 & 0 & 0 & 0 & 0 & 0 \\
0 & 0 & 0 & 0 & 0 & 0 & 0 & 0 & 0
\end{bmatrix} \quad (32)$$

$$\mathbf{A}_{21} = \begin{bmatrix}
\omega_{LP,PLL}\cos(\delta\theta_{PLL,0}-\delta\theta_{VSM,0}) & \omega_{LP,PLL}\sin(\delta\theta_{PLL,0}-\delta\theta_{VSM,0}) & 0 & 0 & 0 & 0 & 0 & 0 & 0 & 0 \\
-\omega_{LP,PLL}\sin(\delta\theta_{PLL,0}-\delta\theta_{VSM,0}) & \omega_{LP,PLL}\cos(\delta\theta_{PLL,0}-\delta\theta_{VSM,0}) & 0 & 0 & 0 & 0 & 0 & 0 & 0 & 0 \\
0 & 0 & 0 & 0 & 0 & 0 & 0 & 0 & 0 & 0 \\
0 & 0 & 0 & 0 & 0 & 0 & 0 & 0 & 0 & 0 \\
-1 & 0 & 0 & 0 & 0 & 0 & -r_v & \omega_g l_v & 0 & 0 \\
0 & -1 & 0 & 0 & 0 & 0 & -\omega_g l_v & -r_v & 0 & 0 \\
-\omega_f i_{o,q,0} & \omega_f i_{o,d,0} & 0 & 0 & 0 & 0 & \omega_f v_{o,q,0} & -\omega_f v_{o,d,0} & 0 & 0 \\
-\frac{i_{o,d,0}}{T_a} & -\frac{i_{o,q,0}}{T_a} & 0 & 0 & 0 & 0 & -\frac{v_{o,d,0}}{T_a} & -\frac{v_{o,q,0}}{T_a} & 0 & 0 \\
0 & 0 & 0 & 0 & 0 & 0 & 0 & 0 & 0 & 0
\end{bmatrix} \quad (33)$$

$$\mathbf{A}_{22} = \begin{bmatrix}
-\omega_{LP,PLL} & 0 & 0 & -\omega_{LP,PLL}\begin{pmatrix}v_{o,q,0}\cos(\delta\theta_{PLL,0}-\delta\theta_{VSM,0})\\ -v_{o,d,0}\sin(\delta\theta_{PLL,0}-\delta\theta_{VSM,0})\end{pmatrix} & 0 & 0 & 0 & 0 & \omega_{LP,PLL}\begin{pmatrix}v_{o,q,0}\cos(\delta\theta_{PLL,0}-\delta\theta_{VSM,0})\\ -v_{o,d,0}\sin(\delta\theta_{PLL,0}-\delta\theta_{VSM,0})\end{pmatrix} \\
0 & -\omega_{LP,PLL} & 0 & \omega_{LP,PLL}\begin{pmatrix}v_{o,d,0}\cos(\delta\theta_{PLL,0}-\delta\theta_{VSM,0})\\ +v_{o,q,0}\sin(\delta\theta_{PLL,0}-\delta\theta_{VSM,0})\end{pmatrix} & 0 & 0 & 0 & 0 & -\omega_{LP,PLL}\begin{pmatrix}v_{o,d,0}\cos(\delta\theta_{PLL,0}-\delta\theta_{VSM,0})\\ +v_{o,q,0}\sin(\delta\theta_{PLL,0}-\delta\theta_{VSM,0})\end{pmatrix} \\
0 & \frac{1}{v_{PLL,d,0}} & 0 & 0 & 0 & 0 & 0 & 0 & 0 \\
0 & 0 & 0 & 0 & 0 & 0 & 0 & \omega_b & 0 \\
0 & 0 & 0 & 0 & 0 & 0 & -k_q & l_v i_{o,q,0} & 0 \\
0 & 0 & 0 & 0 & 0 & 0 & 0 & -l_v i_{o,d,0} & 0 \\
0 & 0 & 0 & 0 & 0 & 0 & -\omega_f & 0 & 0 \\
0 & \frac{k_d k_{p,PLL}}{T_a v_{PLL,d,0}} & \frac{k_d k_{i,PLL}}{T_a} & 0 & 0 & 0 & 0 & -\frac{k_d+k_\omega}{T_a} & 0 \\
0 & \frac{\omega_b k_{p,PLL}}{v_{PLL,d,0}} & \omega_b k_{i,PLL} & 0 & 0 & 0 & 0 & 0 & 0
\end{bmatrix} \quad (34)$$

$$
\mathbf{B} =
\begin{bmatrix}
0 & 0 & 0 & 0 & 0 & \omega_b v_{o,q,0} \\
0 & 0 & 0 & 0 & 0 & -\omega_b v_{o,d,0} \\
0 & \dfrac{\omega_b k_{pc} k_{pv} k_q}{l_f} & 0 & \dfrac{\omega_b k_{pc} k_{pv}}{l_f} & 0 & \dfrac{\omega_b k_{pc}(k_{pv} l_v i_{o,q,0} - c_f v_{o,q,0})}{l_f} \\
0 & 0 & 0 & 0 & 0 & \dfrac{\omega_b k_{pc}(-k_{pv} l_v i_{o,d,0} + c_f v_{o,d,0})}{l_f} \\
0 & k_{pv} k_q & 0 & k_{pv} & 0 & k_{pv} l_v i_{o,q,0} - c_f v_{o,q,0} \\
0 & 0 & 0 & 0 & 0 & -k_{pv} l_v i_{o,d,0} + c_f v_{o,d,0} \\
0 & 0 & -\dfrac{\omega_b \cos(\delta\theta_{VSM,0})}{l_g} & 0 & 0 & \omega_b i_{o,q,0} \\
0 & 0 & \dfrac{\omega_b \sin(\delta\theta_{VSM,0})}{l_g} & 0 & 0 & \omega_b i_{o,d,0} \\
0 & 0 & 0 & 0 & 0 & 0 \\
0 & 0 & 0 & 0 & 0 & 0 \\
0 & 0 & 0 & 0 & 0 & 0 \\
0 & 0 & 0 & 0 & 0 & 0 \\
0 & 0 & 0 & 0 & 0 & 0 \\
0 & 0 & 0 & 0 & 0 & 0 \\
0 & k_q & 0 & 1 & 0 & l_v i_{o,q,0} \\
0 & 0 & 0 & 0 & 0 & -l_v i_{o,d,0} \\
0 & 0 & 0 & 0 & 0 & 0 \\
\dfrac{1}{T_a} & 0 & 0 & 0 & \dfrac{k_\omega}{T_a} & -\dfrac{k_\omega}{T_a} \\
0 & 0 & 0 & 0 & 0 & 0
\end{bmatrix}
\tag{35}
$$

4. Dynamic operation of the reference VSM implementation

The functional behaviour of the reference VSM implementation is illustrated in this section by means of numerical simulations of a few relevant cases. A dynamic model of the investigated system and its corresponding small-signal state-space model have been implemented in Matlab Simulink with the set of parameters listed in Table 1. The parameters of the PI current and voltage controller in this table are obtained by the Modulus Optimum (MO) and Symmetrical Optimum (SO) criteria, respectively, according to the approach explained in [14,39], assuming a switching frequency of 5 kHz. Similarly, the PI controller parameters of the PLL are calculated by the SO criterion assuming a low pass filter with crossover frequency of 500 rad/s. The inertia time constant of the VSM is selected to emulate a SM with an intermediate inertia representative for a distributed generation unit, while the other parameters are selected by experience-based trial-and-error.
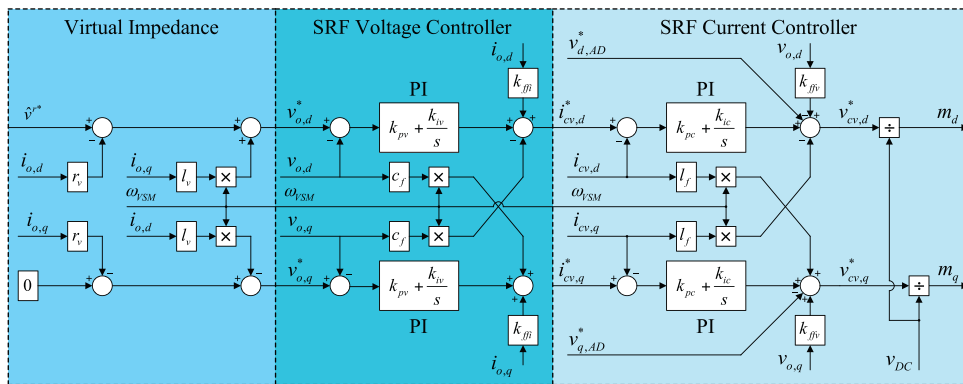

Fig. 6. Virtual inductance, voltage control and current control.
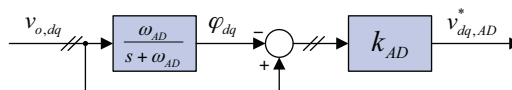

Fig. 7. Implementation of active damping.

Table 1
Parameters of investigated VSM configuration.

Parameter	Value	Parameter	Value
Rated voltage $V_{S,LL,RMS}$	690 V	Filter inductance l_f	0.08 pu
Rated power S_b	2.75 MVA	Filter resistance r_{lf}	0.003 pu
Rated angular frequency ω_b	2π*50 Hz	Filter capacitance c_f	0.074 pu
VSM Inertia constant T_a	2 s	Grid inductance l_g	0.20 pu
VSM Damping coefficient k_d	400	Grid resistance r_g	0.01 pu
Current controller gain: k_{pc}, k_{ic}	1.27, 14.3	Grid voltage $\hat{v}_g$	1.0 pu
Voltage controler gain: k_{pv}, k_{iv}	0.59, 736	Active damping filter ω_{AD}	50 rad/s
Power reference p^*	0.5 pu	Active damping gain k_{AD}	0.5 pu
Frequency droop gain k_ω	20 pu	Virtual Inductance l_v	0.2 pu
Reactive power reference q^*	0.0 pu	Virtual Resistance r_v	0.0 pu
Reactive power droop gain k_q	0.2 pu	PLL filter $\omega_{LP,PLL}$	500 rad/s
Reactive power filter ω_f	1000 rad/s	PLL proportional gain $k_{p,PLL}$	0.084
Voltage reference $\hat{v}^*$	1.02 pu	PLL integral gain $k_{i,PLL}$	4.69

## 4.1. Dynamic response to change in loading

In the first simulated case, the dynamic response of the system is examined for a step in the power reference input to the VSM from 0.5 pu to 0.7 pu when the grid frequency and the reference frequency are both equal to 1.0 pu. This case is equivalent to a sudden increase in the input power or torque on the shaft of a SM connected to an infinite bus.

The power reference and the resulting electrical power from the VSM are plotted in Fig. 8, where it is shown that the VSM with the selected parameters exhibits a smooth transient response and reaches steady state conditions in approximately 1 s without any overshoot. The step change in the reference triggers also a dynamic response in the rotating speed of the virtual inertia, as shown in Fig. 9. Indeed, the excess "mechanical" power input is accumulated in the virtual inertia of the VSM, resulting in an increasing speed during the first part of the transient. This leads to an increase in the phase angle between the VSM-oriented reference frame and the grid voltage vector as shown in the upper part of Fig. 10, until the electrical power output from the machine balances its "mechanical" input. When the electrical power reaches the input power and the steady-state power balance of the system is restored, the rotational speed of the virtual inertia returns to the synchronous speed of the grid source, just as for a traditional SM.

The transient behaviour shown in the presented curves exhibits the same general characteristics as for a conventional SM, but with a more damped response. Indeed, the VSM replicates the behaviour of a classical SM, but its parameters do not have to comply with any
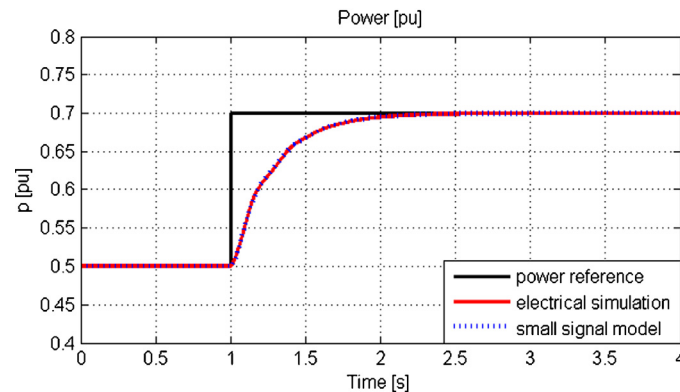
Fig. 8. Response of nonlinear model and linearized small-signal model to a step in the power reference input.
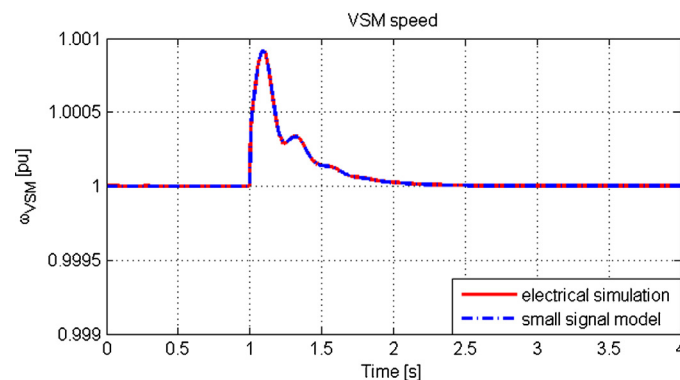
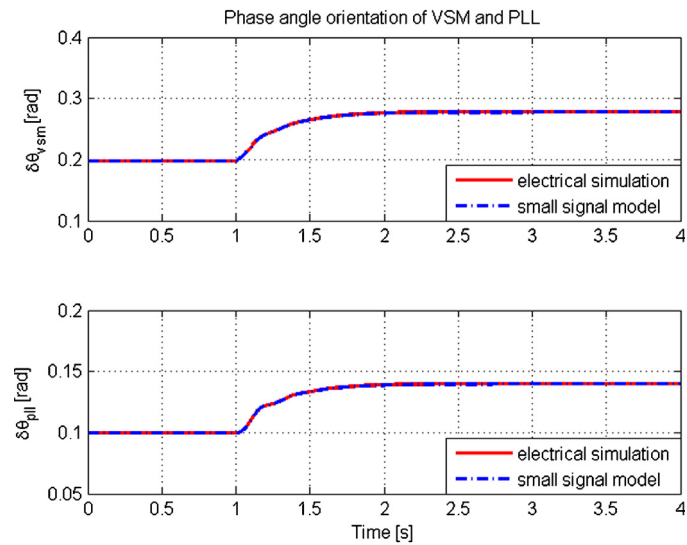**Fig. 9.** Response of the VSM speed to a step in the power input.

Fig. 10. Phase angle displacements of the VSM and PLL reference frames with respect to the grid voltage in response to the step in power reference.

physical design constraint. Thus, the parameters of the VSM can be selected with more freedom, without considering any efficiency aspects. In particular, power losses due to the damping effects of the VSM appear only in the control system and not in any physical circuit.

The reference frame orientation of the PLL with respect to the grid voltage vector is shown in the lower part of Fig. 10, illustrating how the phase angle of the voltage at the filter capacitors is changing with the power flow due to the grid impedance. However, it is noticeable how the phase angle of the VSM changes more than for the PLL, due to the virtual inductance included in the VSM. Thus, the VSM phase angle can be considered as equivalent to the phase angle of the internal voltage behind the synchronous reactance of a traditional SM, while the PLL is tracking the phase angle of the voltage at the terminals of the VSM.

The reactive power flow from the VSM is shown in Fig. 11, to illustrate the very small change in the reactive power flow due to the droop controller's response to the change of operating conditions when the active power flow is changed. The plot also indicates small oscillation at a relatively high frequency. This response is mainly due to the response of the LC filter and the measurement filter used in the droop controller.

The presented figures include results from simulation of the non-linear model of the VSM as well as results from simulating the same events with the linearized small-signal state-space model in the same plots. It can be observed that all the curves indicate an excellent match between the two models, for both the fast and slow transients in the system, as long as the operating point stays close enough to the linearization point. This verifies the validity of the linearized model around the steady-state operating point, and indicates that it can be used for investigating system stability and the influence of parametric variations by traditional techniques for linear system analysis.

4.2. Response to change in the grid frequency

The results from an additional simulation case are shown in Figs. 12 and 13, where the grid frequency of the system is ramped down from 1.0 pu to 0.995 pu as shown in the upper part of Fig. 12. Due to this change of grid frequency, the frequency droop gain specified by k_ω is activated and the VSM increases its power output in steady state. The VSM speed follows the grid frequency, releasing energy from its inertia corresponding to the change of speed, and settles at the new operating frequency of the grid with increased power output to contribute to the frequency control of the power system. This can also be seen from the power flow in Fig. 12 and the corresponding converter currents in Fig. 13.

However, for the linearized small signal model, it should be remembered that the speed deviation from the linearization point in steady state must be zero for the phase angle specified by (5) to settle to a constant value. This implies that the linearized model of the VSM
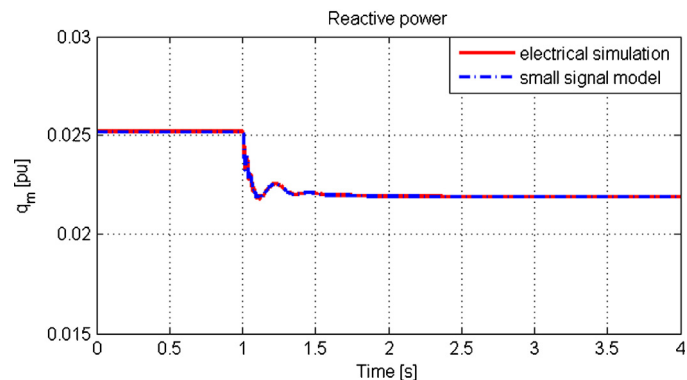

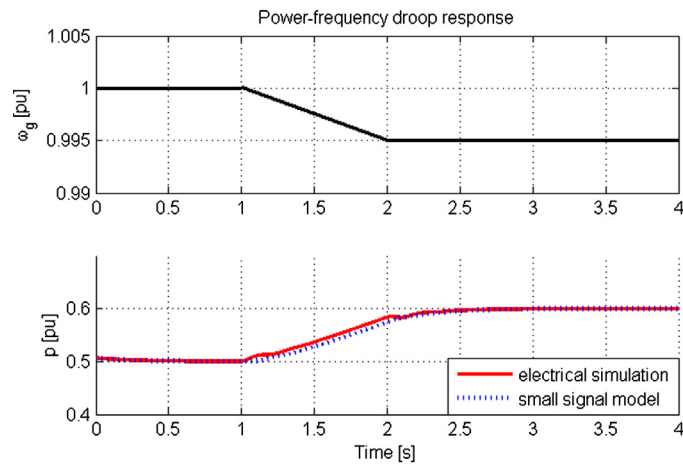**Fig. 11.** Response of reactive power flow to the step in active power reference.

Fig. 12. Response of the VSM power flow to a change in the grid frequency.
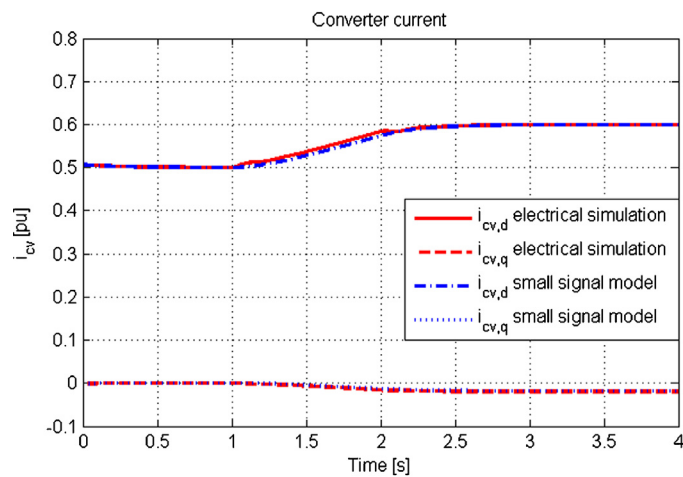

Fig. 13. Converter currents as a response to the change of operating conditions when the grid frequency changes.

connected to an infinite bus cannot correctly represent the dynamic transition into a new operating point with a different grid frequency than at the linearization point. Thus, a small deviation between the non-linear and linearized models can be observed while the frequency is changing and for a short transient after the frequency has settled to its new steady-state value, as shown by the curves in Figs. 12 and 13. This is because the grid frequency is not a state variable in the developed small-signal model. Still, the contribution from the change of grid frequency through the B-matrix from (35) is able to represent the corresponding change of power flow also for the linearized model. Thus, the results presented in Figs. 12 and 13 are demonstrating that the VSM is operating as intended, while at the same time revealing some of the limitations of the developed small-signal model.

4.3. System eigenvalue analysis

Since the developed linearized small-signal model has been shown to accurately represent the investigated system for small deviations around the linearization point, the eigenvalues of the **A** matrix can be calculated to systematically identify all the modes of the system. The resulting system eigenvalues for the operating point corresponding to the conditions given in Table 1 are listed in Table 2.

For assessing the system stability, the slow and poorly damped poles are of main interest. It can be noticed from the eigenvalues in Table 2, that the system has several real poles close to the origin and two pairs of complex conjugate poles with small real parts and low oscillation frequency. There are also two pairs of high frequency poles, and one pair of fast poles close to the real axis.

Table 2
System eigenvalues.

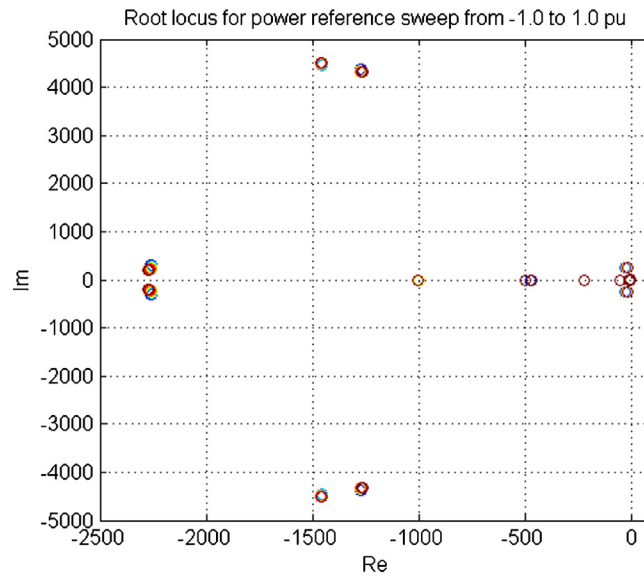|	
$\lambda_1 = -500$	$\lambda_{12} = -224$
$\lambda_{2,3} = -1460 \pm j\,4498$	$\lambda_{13,14} = -6.8 \pm j\,26.4$
$\lambda_{4,5} = -1272 \pm j\,4329$	$\lambda_{15} = -50.8$
$\lambda_{6,7} = -2262 \pm j\,225$	$\lambda_{16} = -50.6$
$\lambda_8 = -1002$	$\lambda_{17} = -37.0$
$\lambda_9 = -470$	$\lambda_{18} = -11.2$
$\lambda_{10,11} = -19.5 \pm j\,245$	$\lambda_{19} = -11.2$

Fig. 14. Root locus of all system poles when the power reference p^* is swept through the full operating range of the VSM.
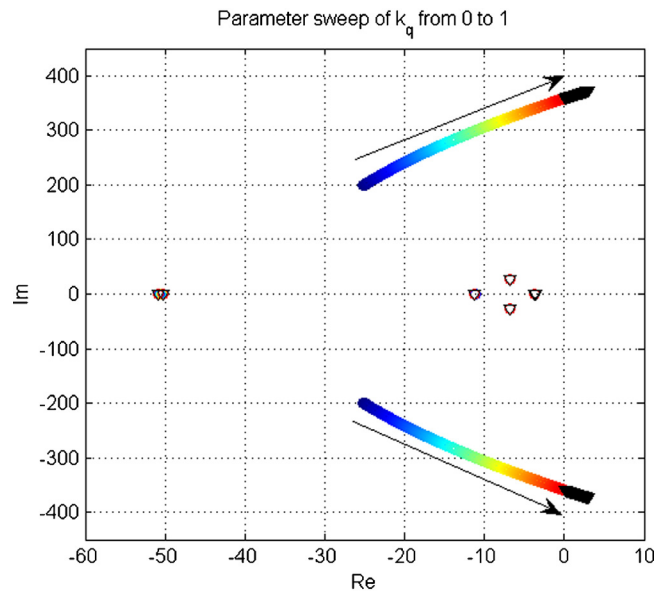

Fig. 15. Root locus of the poles closest to the imaginary axis when the reactive power droop gain k_q is swept from 0 to 1.

As already seen, the system is stable with the parameters and operating conditions specified in Table 1. Since the small signal model has been shown to accurately represent the system around the linearization point, the system stability for the full operation range of the VSM has been investigated by plotting the system poles when the power reference p^* is swept from −1.0 pu to 1.0 pu. This corresponds to all the steady state operating conditions of the system that can be found by solving the nonlinear model from (28) as a function of the power reference while all other parameter values are as specified in Table 1. The result is shown in Fig. 14, where it can be seen that none of the system poles are moving much when the steady state operating conditions are changed. This indicates that the VSM will exhibit similar dynamic response as already discussed for its entire allowed operating range.

Although the system is stable for the full range of operating conditions with the parameters and operating conditions from Table 1, it should be noted that the stability can still be sensitive to variations in the system parameters. For instance, an investigation of a similar configuration reported in [14] indicated that stable operation of the system will be challenging if the switching frequency and thus the bandwidth of the inner loop current controllers is low. In such a case, or due to other changes in the parameters of the inner loop controllers, the poles with the highest imaginary parts, which are associated with the LC filter of the system, can easily move into the right half-plane and cause instability.

There are also other potential parameters that can cause instability in the system under certain conditions. As an example, the trajectory of the poles closest to the imaginary axis are shown in Fig. 15 when the reactive power droop gain k_q is swept from 0 to 1.0. The change of the pole location is indicated with a colour gradient, starting from blue when k_q is 0 and changing towards red as k_q increases. It can be seen from the figure that one pair of complex conjugate poles are moving towards the imaginary axis, and are causing instability when k_q becomes too high. Similar investigations of stability limitations can easily be carried out for any of the system parameters, and can be used
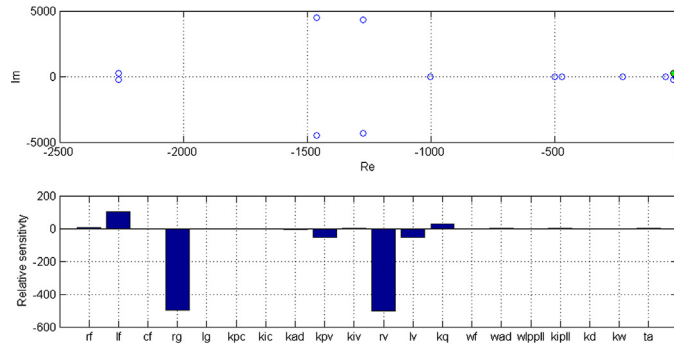
Fig. 16. Parametric sensitivity of the pole resulting in instability with high values of k_q.
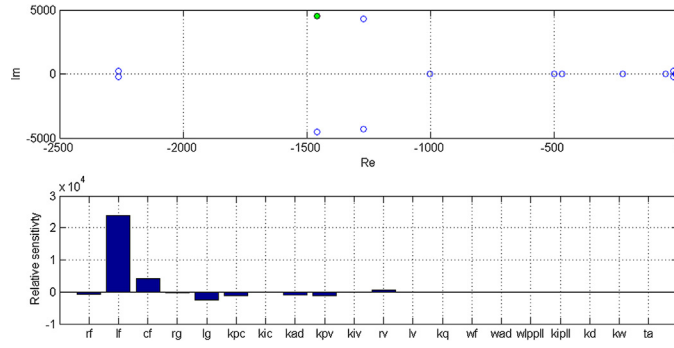

Fig. 17. Parametric sensitivity of the pole with the highest imaginary part.

to support the tuning of the controllers as long as one single or a few clearly identified parameters are responsible for the stability problems in a particular system configuration. Such studies can be of high importance, considering the utilization of the VSM in a SmartGrid scenario with large expected variations in grid configurations, operating conditions and system parameters.

4.4. Parametric sensitivity of critical poles

Investigation of the system stability by ad hoc variations of the controller parameters is challenging for a high order system as the investigated VSM, especially if several parameters are influencing the same pole. To more easily identify the parameters that should be modified to improve the stability and dynamic performance of the system, the parameter sensitivity of pole locations can instead be studied.

The parameter sensitivity of the system poles is defined as the derivative of the eigenvalues with respect to the system parameters. For a dynamic system of order N and with a set of K tunable parameters, the sensitivities define a sensitivity matrix of N by K complex elements. The relative sensitivity $\alpha_{n,k}$ of the parameter ρ_k with respect to the eigenvalue n can be expressed by (36), where Ψ_n^T and Φ_n are the left and right eigenvectors associated to the eigenvalue λ_n [14,30]:

$$\alpha_{n,k} = \frac{\partial \lambda_n}{\partial \rho_k} = \frac{\Phi_n^T \frac{\partial \mathbf{A}}{\partial \rho_k} \Psi_n}{\Phi_n^T \Psi_n} \tag{36}$$

The real part of these sensitivities is directly associated to the derivatives of the pole location along the real axis with respect to each parameters. Thus, a positive value means that the investigated pole will be moved towards the right by an increase of the corresponding parameter. Similarly, the imaginary part of the sensitivity is associated with the derivative of the pole location along the imaginary axis. However, since the real parts of the pole locations determine the stability and corresponding time constant of the associated system mode, only the real part of the sensitivity matrix is investigated here.

An example of parametric sensitivity analysis for the pole causing instability in Fig. 15 is shown in Fig. 16. From this figure it can be seen that the investigated pole is mainly sensitive to the resistance in the grid and the virtual resistance of the VSM. However, the grid resistance cannot be influenced by the VSM and the virtual resistance should preferably be kept at a low value to achieve a good decoupling of the active and reactive power control of the VSM. Also the actual filter inductance of the converter and the virtual inductance of the VSM have some impact on this pole, but as the grid inductance cannot be influenced by the VSM only the virtual inductance can be modified to improve the stability and dynamic response of the system. The parameter sensitivity also proves that the reactive power droop gain k_q has an influence on the pole, and that reducing the droop gain would help to move the pole towards the left. It can also be noticed that an increase of the voltage controller gain k_{pv} can bring the pole towards the left, while all other adjustable parameters have negligible influence on the pole location. Thus, the main parameters that can be used to influence the location of this pole are the droop gain, the voltage controller gain and the virtual inductance.

Another example of a parameter sensitivity analysis is shown in Fig. 17, for the pole with the highest imaginary part. This is one of the poles that can cause instability due to resonance in the LC filter, even if it is very well damped in this case due to the implemented active damping algorithm. It can, however, be seen that it is sensitive to the physical parameters of the LC filter and the grid, and it is also clear

that the location of this pole can be influenced by the proportional gains of the voltage and current controllers, as well as the gain of the active damping algorithm k_{AD}.

In case of stability problems in the system, such parameter sensitivity analysis can be easily performed for any of the implicated poles. However, it should be remembered that the change of a parameter to improve the stability conditions or dynamic response associated with one pole, might move another pole in the wrong direction. If that is the case, manual tuning of the controller parameters might be challenging even with support from parameter sensitivity analysis. However, as proposed in [14], it is possible to design automated iterative procedures that can help to bring the pole locations of the system into stable conditions with improved dynamic response. Such approaches might be necessary if a high order system like the investigated VSM is interfaced with other dynamic models and the interaction between the states in the various parts of the overall system model is causing instabilities or poorly damped dynamic responses. The presented VSM model and the tools applied to analyze the properties of the investigated configuration provide a starting point for studying the operation of VSM performance in a larger scale system as will be the case in a SmartGrid scenario.

5. Conclusion

The concept of a Virtual Synchronous Machine (VSM) as an approach for controlling power electronics converters to replicate the behavioural characteristics of Synchronous Machines (SMs) has been introduced during the last decade. This paper has highlighted the inherent advantages of the VSM as a possible alternative for releasing the potential advantages of distributed autonomous control actions of power electronics converters in the SmartGrid context. An implementation of the VSM concept based on an emulated swing equation providing references for cascaded voltage and current controllers has been presented in detail. In particular, a nonlinear mathematical model of the investigated VSM scheme, and its linearized small-signal equivalent, has been derived. These models have been simulated numerically in order to verify and illustrate the behaviour of the VSM and a few of its inherent features. Finally, the system eigenvalues and their parametric sensitivities have been analyzed for the linearized system in order to provide further insight into the dynamic properties and stability characteristics of this VSM implementation. Thus, in addition to the detailed description of a VSM implementation suitable for power system applications in the SmartGrid context, the paper has also presented and verified the models needed for accurately representing the impact of this VSM implementation on the power system in larger scale small-signal power system stability studies.

Acknowledgement

References

[1] CIRED Working Group on Smart Grids, Smart Grids on the Distribution Level – Hype or Vision? CIRED's Point of View, Final Report, 2013, Available at: http://www.cired.at/pdf/CIRED_WG_SmartGrids_FinalReport.pdf

[2] European Center for Power Electronics, ECPE, European Power Electronics and Drives Association, EPE, Position Paper on Energy Efficiency – The Role of Power Electronics, 2007, Available at: http://www.ecpe.org/securedl/0/1391290694/35ad20b5395221115c886f006df4d0f595ed7174/fileadmin/user_upload/Public_Relations/ECPE_Publications/ECPE_Position_Paper_Energy_Efficiency.pdf

[3] J. Morren, J. Pierik, S.W.H. de Haan, Inertial response of variable speed wind turbines, Electr. Power Syst. Res. 76 (July (11)) (2006) 980–987.

[4] H.-P. Beck, R. Hesse, Virtual synchronous machine, in: Proc. of the 9th Int. Conf. on Electrical Power Quality and Utilisation, Barcelona, Spain, 9–11 October, 2007, 6 pp.

[5] J. Zhu, C.D. Booth, G.P. Adam, A.J. Roscoe, C.G. Bright, Inertia emulation control strategy for VSC-HVDC transmission systems, IEEE Trans. Power Syst. 28 (May (2)) (2013) 1277–1287.

[6] Z. Linn, Y. Miura, T. Ise, Power system stabilization control by HVDC with SMES using virtual synchronous generator, IEEJ J. Ind. Appl. 1 (2) (2012) 102–110.

[7] T. Shintai, Y. Miura, T. Ise, Reactive power control for load sharing with virtual synchronous generator control, in: Proc. of the IEEE 7th Int. Power Electronics and Motion Control Conference – ECCE Asia, Harbin, China, 2–5 June 2012, 2012, pp. 846–853.

[8] J. Driesen, K. Visscher, Virtual synchronous generators, in: Proc. of the IEEE Power and Energy Society 2008 General Meeting: Conversion and Delivery of Energy in the 21st Century, Pittsburgh, PA, USA, 20–24 July, 2008, 3 pp.

[9] Q.-C. Zhong, G. Weiss, Synchronverters: inverters that mimic synchronous generators, IEEE Trans. Ind. Electron. 58 (April (4)) (2011) 1259–1267.

[10] S. D'Arco, J.A. Suul, Virtual Synchronous Machines – classification of implementations and analysis of equivalence to droop controllers for microgrids, in: Proc. of IEEE PowerTech Grenoble 2013, Grenoble, France, 16–20 June 2013, 2013, 7 pp.

[11] K. Visscher, S.W.H. De Haan, Virtual Synchronous Machines (VSG's) for frequency stabilization in future grids with a significant share of decentralized generation, in: Proc. of the CIRED Seminar 2008: SmartGrids for Distribution, Frankfurt, Germany, 23–24 June 2008, 2008, 4 pp.

[12] K. Sakimoto, Y. Miura, T. Ise, Stabilization of a power system with a distributed generator by a virtual synchronous generator function, in: Proc. of the 8th Int. Conference on Power Electronics – ECCE Asia, Jeju, Korea, 30 May–3 June 2011, 2011, 8 pp.

[13] H. Bevrani, T. Ise, Y. Miura, Virtual synchronous generators: a survey and new perspectives, Int. J. Electr. Power Energy Syst. 54 (2014) 244–254.

[14] S. D'Arco, J.A. Suul, O.B. Fosso, Control system tuning and stability analysis of Virtual Synchronous Machines, in: Proc. of the 2013 IEEE Energy Conversion Congress and Exposition, ECCE 2013, Denver, CO, USA, 15–19 September 2013, 2013, pp. 2664–2671.

[15] S. D'Arco, J.A. Suul, O.B. Fosso, Small-signal modelling and parametric sensitivity of a Virtual Synchronous Machine, in: Proc. of the 18th Power Systems Computational Conference, PSCC, Wrocław, Poland, 18–22 August 2014, 2014, 9 pp.

[16] F. Blaabjerg, R. Teodorescu, M. Liserre, A.V. Timbus, Overview of control and grid synchronization for distributed power generation systems, IEEE Trans. Ind. Electron. 53 (October (5)) (2006) 1398–1409.

[17] J. Rocabert, A. Luna, F. Blaabjerg, P. Rodríguez, Control of power converters in AC microgrids, IEEE Trans. Power Electron. 27 (November (11)) (2012) 4734–4749.

[18] D. Pudjianto, C. Ramsay, G. Strbac, Virtual power plant and system integration of distributed energy resources, IET Renew. Power Gener. 1 (March (1)) (2007) 10–16.

[19] E.A. Setiawan, Concept and Controllability of Virtual Power Plant (Dr. Ing thesis), Kassel University, Kassel, Germany, 2007.

[20] J. Hansen et al., Providing Flexibility with a Virtual Power Plant, Final Demo Report, Deliverable No: 10.3, Twenties Project. Available at: http://www.twenties-project.eu/system/files/D10.3_Providing%20flexibility%20with%20a%20virtual%20power%20plant.pdf

[21] T.L. Vandoorn, J.D.M. De Kooning, B. Meersman, L. Vandevelde, Review of primary control strategies for islanded microgrids with power-electronic interfaces, Renew. Sustain. Energy Rev. 19 (2013) 613–628.

[22] T.L. Vandoorn, B. Zwaenepoel, J.D.M. De Kooning, B. Meersman, L. Vandevelde, Smart microgrids and virtual power plants in a hierarchical control structure, in: Proc. of the 2nd IEEE PES Int. Conference and Exhibition on Innovative Smart Grid Technologies, ISGT Europe 2011, Manchester, UK, 5–7 December 2011, 2011, 7 pp.

[23] J. Machowski, J.W. Bialek, J.R. Bumby, Power System Dynamics and Stability, Wiley, Chichester, UK, 1997 (Chapters 2 and 5).

[24] R. Hesse, D. Turschner, H.-P. Beck, Micro grid stabilization using the Virtual Synchronous Machine (VISMA), in: Proc. of the Int. Conference on Renewable Energies and Power Quality, ICREPQ'09, Valencia, Spain, 15–17 April 2009, 2009, 6 pp.

[25] Y. Chen, R. Hesse, D. Turschner, H.-P. Beck, Dynamic properties of the Virtual Synchronous Machine (VSIMA), in: Proc. of the Int. Conference on Renewable Energies and Power Quality, ICREPQ'11, Las Palmas, Spain, 13–15 April 2011, 2011, 5 pp.

[26] Y. Chen, R. Hesse, D. Turschner, H.-P. Beck, Investigation of the Virtual Synchronous Machine in the Island Mode, in: Proc. of the 2012 3rd IEEE Innovative Smart Grid Technologies Conference – Europe, ISGT Europe, Berlin, Germany, 15–17 October 2012, 2012, 6 pp.

[27] N. Pogaku, M. Prodanović, T.C. Green, Modeling, analysis and testing of autonomous operation of an inverter-based microgrid, IEEE Trans. Power Electron. 22 (March (2)) (2007) 613–625.

[28] S. D'Arco, G. Guidi, J.A. Suul, Embedded limitations and protections for droop-based control schemes with cascaded loops in the synchronous reference frame, in: Proc. of the 2014 Int. Power Electronics Conference, IPEC-Hiroshima 2014 – ECCE Asia, Hiroshima, Japan, 18–21 May 2014, 2014, pp. 1544–1551.

[29] S. D'Arco, J.A. Suul, Equivalence of Virtual Synchronous Machines and frequency-droops for converter-based MicroGrids, IEEE Trans. Smart Grid 5 (January (1)) (2014) 394–395.

[30] P. Kundur, Power System Stability and Control, McGraw-Hill, New York, 1994.

[31] V. Kaura, V. Blasko, Operation of a phase locked loop system under distorted utility conditions, IEEE Trans. Ind. Appl. 33 (January/February (1)) (1997) 58–63.

[32] H. Kolstad, Control of an Adjustable Speed Hydro utilizing Field Programmable Devices (Ph.D. thesis), Norwegian University of Science and Technology, 2002.

[33] A. Haddadi, G. Joos, Load Sharing of Autonomous Distribution-level Microgrids, in: Proc. 2011 IEEE PES General Meeting: The Electrification of Transportation and the Grid of the Future, Detroit, MI, USA, 24–28 July 2011, 2011, 9 pp.

[34] J. He, Y.W. Li, Analysis, design, and implementation of virtual impedance for power electronics interfaced distributed generation, IEEE Trans. Ind. Appl. 47 (November/December (6)) (2011) 2525–2538.

[35] V. Blasko, V. Kaura, A new mathematical model and control of a three-phase AC–DC voltage source converter, IEEE Trans. Power Electron. 12 (January (1)) (1997) 116–123.

[36] M. Malinowski, M.P. Kazmierkowski, S. Bernet, New simple active damping of resonance in three-phase PWM converter with LCL filter, in: Proc. of the 2005 IEEE Int. Conference on Industrial Technology, ICIT 2005, Hong Kong, 14–17 December 2005, 2005, pp. 861–865.

[37] N. Kroutikova, C.A. Hernandez-Aramburo, T.C. Green, State-space model of grid-connected inverters under current control mode, IET Electr. Power Appl. 1 (May (3)) (2007) 329–338.

[38] S. D'Arco, J.A. Suul, O.B. Fosso, Small-signal modelling and parametric sensitivity of a Virtual Synchronous Machine in islanded operation, Int J Elec Power (2014), accepted for publication.

[39] C. Bajracharya, M. Molinas, J.A. Suul, T.M. Undeland, Understanding of tuning techniques of converter controllers for VSC-HVDC, in: Proc. of Nordic Workshop on Power and Industrial Electronics, NORPIE 2008, Espoo, Finland, 9–11 June, 2008, 2008, 8 pp.